

compared to the amount of exhumation and explains why Denali is so high. If we consider the central Alaska Range as a whole, rather than the immediate Denali area, assuming that the fission-track data from Denali apply to the whole range, mean surface elevation is ~1 km and the amount of tectonic uplift is ~1.7 km. This calculation is a limiting case because the timing of uplift and the amount of uplift and exhumation may vary, for example, with distance from the DFS. Pebble studies in the Nenana Gravels indicate that uplift and exhumation started in the south and proceeded northward (18).

North to northwest motion of the Kula and Pacific plates relative to the North America plate in the late Cretaceous to Holocene provides a driving force for dextral movement along the DFS (2). In a model for the uplift and exhumation of the central Alaska Range, the arcuate geometry of the DFS (especially the bend in fault trend near Denali) plus the close proximity of Denali to the DFS must be considered. At some active margins, oblique convergence is accommodated by strike-normal compression and strike-parallel translation (19). Dextral transpressive movement along the DFS forces rocks outboard of the fault against the bend and the Yukon-Tanana terrane. Sediments in the Healy Basin and the fission-track data indicate that, at least from ~16 to 6 Ma, this transpressive movement resulted in little, if any, uplift and exhumation of Denali. An acceleration in lateral movement along the DFS or an increase in compressive force could conceivably create space problems at the bend in the fault trend and cause uplift. Relative plate motion vectors calculated for three azimuths of the McKinley strand suggest that, at ~5 or 6 Ma, the tangential component at Denali and the Kichatna Mountains changed direction from dextral to sinistral (Fig. 4). However, the tangential component at Mount Deborah remained dextral. This geometry created a situation in which tangential motion vectors opposed each other along different segments of the fault. In all cases the normal component increased; this change would amplify the space problem and force the intervening crustal blocks upward. The magnitudes of the components are maxima because the outboard collage of terranes probably absorbed some of the strain, and it is unlikely that plate coupling was 100% efficient. The vector resultants are supported by regional paleomagnetic evidence: counterclockwise rotations of individual southwestern Alaska terranes (20) could be favored by a temporary, localized sinistral regime. In this context, the observed drainage patterns surrounding the Denali massif that imply right-lateral movement might be attributed to counterclockwise rota-

tion of blocks during uplift and exhumation.

In conclusion, existing geologic, thermochronometric, and paleogeographic data indicate that Denali was rapidly uplifted at ~6 Ma. This uplift was perhaps a direct result of the space problem caused by the ~5 Ma change in motion of the Pacific plate interacting with the DFS.

REFERENCES AND NOTES

- P. J. Coney, D. L. Jones, J. W. H. Monger, *Nature* **288**, 329 (1980).
- D. C. Engrebretson, A. Cox, R. G. Gordon, *Geol. Soc. Am. Spec. Pap.* **206** (1985).
- D. G. Howell, Ed., *Tectonostratigraphic Terranes of the Circum-Pacific Region* (Circum-Pacific Council for Energy and Mineral Resources, Earth Sciences series, Houston, 1985).
- D. L. Jones, N. J. Siberling, W. Gilbert, P. J. Coney, *J. Geophys. Res.* **87**, 3709 (1982).
- P. J. Coney and D. L. Jones, *Tectonophysics* **119**, 265 (1985).
- B. Csejtey, D. P. Cox, R. C. Evarts, G. D. Stricker, H. L. Foster, *J. Geophys. Res.* **87**, 3741 (1982).
- J. H. Stout and C. G. Chase, *Can. J. Earth Sci.* **17**, 1527 (1980).
- G. E. Brogan, L. S. Cluff, M. K. Korrington, D. B. Slemmons, *Tectonophysics* **29**, 73 (1975); M. A. Lanphere, *Can. J. Earth Sci.* **15**, 817 (1978); C. Wahrhaftig, D. L. Turner, F. R. Weber, T. E. Smith, *Geology* **3**, 463 (1975); R. G. Hickman, K. W. Sherwood, C. Craddock, *Tectonics* **9**, 1433 (1990).
- B. L. Reed and M. A. Lanphere, *Geol. Soc. Am. Bull.* **85**, 1883 (1974); R. G. Hickman, K. W. Sherwood, C. Craddock, *ibid.* **88**, 1217 (1977).
- B. L. Reed and M. A. Lanphere, *ibid.*, p. 2583; M. A. Lanphere and B. L. Reed, *J. Geophys. Res.* **90**, 11413 (1985).
- R. W. Brown, *Geology* **19**, 74 (1991).
- P. F. Green, I. R. Duddy, A. J. W. Gleadow, P. R. Tingate, G. M. Laslett, *Isot. Geosci.* **59**, 237 (1986).
- A. J. W. Gleadow, I. R. Duddy, P. F. Green, J. F. Lovering, *Contrib. Mineral. Petrol.* **94**, 405 (1986); P. F. Green *et al.*, *Isot. Geosci.* **79**, 155 (1989).
- P. G. Fitzgerald and A. J. W. Gleadow, *Nucl. Tracks Radiat. Meas.* **17**, 351 (1990).
- Apatite fission-track analysis measures the displacement of rock with respect to a thermal reference frame. On the basis of various assumptions, the rate and magnitude of displacements determined with this technique place constraints on the magnitude of displacements with respect to the geoid or mean sea level (11). The following definitions are used [P. England and P. Molnar, *Geology* **18**, 1173 (1990)]: surface uplift is the displacement of Earth's surface with respect to mean sea level; uplift is the displacement of rock with respect to mean sea level; exhumation (erosion or removal of overburden due to tectonic processes) is the displacement of rock with respect to the surface. Surface uplift is uplift minus exhumation.
- D. B. Dickey, *Sediment. Geol.* **38**, 443 (1984).
- C. Wahrhaftig, J. A. Wolfe, E. B. Leopold, M. A. Lanphere, *U.S. Geol. Surv. Bull.* **1274-D** (1969).
- C. Wahrhaftig, *Geol. Soc. Am. Spec. Pap.* **151** (1975), p. 188.
- M. E. Beck, *Tectonics* **5**, 49 (1986).
- R. S. Coe, B. R. Globberman, P. W. Plumley, G. A. Thrupp, in (3), pp. 85-108.
- A. J. Hurford and P. F. Green, *Isot. Geosci.* **1**, 258 (1983); P. F. Green, *Nucl. Tracks Radiat. Meas.* **5**, 77 (1981).
- Mugs Stump, C. Anker, and P.G.F. collected the samples. We thank the staff of Denali National Park and members of the High Altitude Medical Research Camp for assistance during the summer of 1989. Samples were irradiated at the Georgia Institute of Technology reactor. We thank R. Grimm, S. Peacock, and S. Reynolds for discussion and two anonymous reviewers whose suggestions improved this manuscript. Supported by National Science Foundation grant DPP 8821937. This study is dedicated to the memory of Mugs Stump, killed while guiding on the south buttress of Denali, 21 May 1992.

27 August 1992; accepted 2 November 1992

Seismic Structure of the Southern East Pacific Rise

R. S. Detrick, A. J. Harding, G. M. Kent, J. A. Orcutt, J. C. Mutter, P. Buhl

Seismic data from the ultrafast-spreading (150 to 162 millimeters per year) southern East Pacific Rise show that the rise axis is underlain by a thin (less than 200 meters thick) extrusive volcanic layer (seismic layer 2A) that thickens rapidly off axis. Also beneath the rise axis is a narrow (less than 1 kilometer wide) melt sill that is in some places less than 1000 meters below the sea floor. The small dimensions of this molten body indicate that magma chamber size does not depend strongly on spreading rate as predicted by many ridge-crest thermal models. However, the shallow depth of this body is consistent with an inverse correlation between magma chamber depth and spreading rate. These observations indicate that the paradigm of ridge crest magma chambers as small, sill-like, mid-crustal bodies is applicable to a wide range of intermediate- and fast-spreading ridges.

Current models of crustal magma bodies at mid-ocean ridges, as well as the variation in shallow crustal structure with age, have been strongly influenced by a series of seismic experiments that have been carried out over the past decade along a small section of the northern East Pacific Rise (EPR) between 9°N and 13°N (1-9). Seismic reflection profiles have imaged a narrow (<1 to 4 km wide), thin (tens to hundreds of

meters), sill-like magma body 1 to 2 km below the ridge axis in this area (3, 10, 11).

R. S. Detrick and G. M. Kent, Department of Geology and Geophysics, Woods Hole Oceanographic Institution, Woods Hole, MA 02543.
A. J. Harding and J. A. Orcutt, Scripps Institution of Oceanography, University of California, San Diego, La Jolla, CA 92093.
J. C. Mutter and P. Buhl, Lamont-Doherty Geological Observatory, Columbia University, Palisades, NY 10964.

This magma lens lies at the top of a much broader seismic low-velocity zone with relatively high *P*-wave velocities and low attenuation. This zone has been interpreted as the largely solidified plutonic section of the oceanic crust that contains at most a small fraction of partial melt (5–9). These results suggest that ridge-crest magma chambers are thin, narrow, mid-crustal bodies of melt and crystal mush rather than large, essentially molten reservoirs (12). However, there are few seismic constraints on the dimensions of mid-ocean ridge magma chambers outside of this one area on the northern EPR. In this report we describe results from a combined two-ship multichannel seismic reflection and refraction experiment along the southern EPR carried out in April and May 1991 (Fig. 1). This portion of the EPR is spreading at a total opening rate of 150 to 162 mm year⁻¹ (13). This rate is ~40% faster than that in the area from 9°N to 13°N and close to the fastest spreading rate found anywhere along the global mid-ocean ridge system.

The tectonic setting of the EPR south of the Garrett fracture zone where this experiment was carried out has been well established from Sea Beam and Sea MARC II surveys of the axial region and from extensive dredging (14–16). Our seismic survey was concentrated in three areas centered at 14°15'S, 17°20'S, and over the 15°55'S overlapping spreading center (OSC). A series of reconnaissance reflection profiles were also obtained along and across the rise axis from the northern limb of the large propagator-overlapper at 20.7°S to the Garrett transform, a distance of >800 km (Fig. 1). Three types of seismic data were obtained: (i) common midpoint reflection data, (ii) two-ship expanding spread profiles, and (iii) ocean bottom seismic refraction data. The reflection data were acquired by the research vessel *Maurice Ewing* of Lamont-Doherty Geological Observatory with a 20-gun, 8385-cubic-inch air gun array and a 4-km-long, 160-channel digital streamer. Twenty-three expanding-spread profiles were obtained in the 14°15'S and 17°20'S areas. They were oriented parallel to the rise axis and were shot with a six-gun, 2850-cubic-inch air gun array aboard the research vessel *Thomas Washington* of Scripps Institution of Oceanography and received by the *Ewing's* streamer. Six Scripps ocean bottom seismometers were also deployed in each of three detailed survey areas and recorded both *Ewing* and *Washington* shots for subsequent tomographic studies of the structure of the rise axis. Single-ship stacked and migrated time sections, together with the analysis of a rise axis refraction profile, form the basis of our preliminary observations. We processed the reflection and refraction data according to

the same procedure used in our earlier northern EPR studies (3, 5, 11, 17).

The southern EPR crest in the 14°S area has a broad, dome-shaped bathymetric cross section with relatively subdued flanking topography. Two distinct intracrustal reflectors appear on profiles that were shot along and across the rise axis (Fig. 2). The shallowest reflector is located ~150 ms (two-way travel time) below the sea floor at the ridge crest. It can be traced along the rise axis as a continuous, flat-lying event

that parallels the sea floor. On cross-axis profiles this event is marked by a series of discontinuous, hyperbolic events that deepen to ~300 ms below basement and then become approximately parallel to the sea floor (Fig. 3). The rapid deepening of this event in the first kilometer away from the rise axis is particularly well illustrated in the migrated section shown in Fig. 4. A similar event has been observed in multichannel reflection data on the northern EPR by Harding and colleagues (17, 18) and by

Fig. 1. Tectonic map of the southern EPR showing the location of the major segment boundaries (16). The combined seismic reflection and refraction experiment reported here was primarily concentrated in three areas centered at 14°15'S, 17°20'S, and over the 15°55'S OSC. However, a series of reconnaissance reflection profiles was obtained along and across the rise axis from the northern limb of the 20.7°S propagator to the Garrett fracture zone. The gray band along the rise axis indicates those portions of the ridge associated with an axial magma chamber (AMC) reflection.

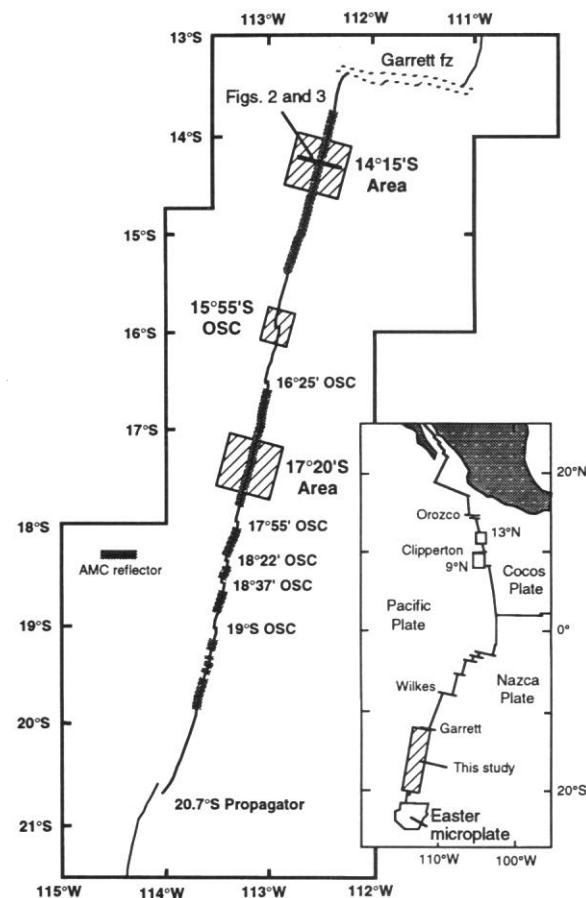
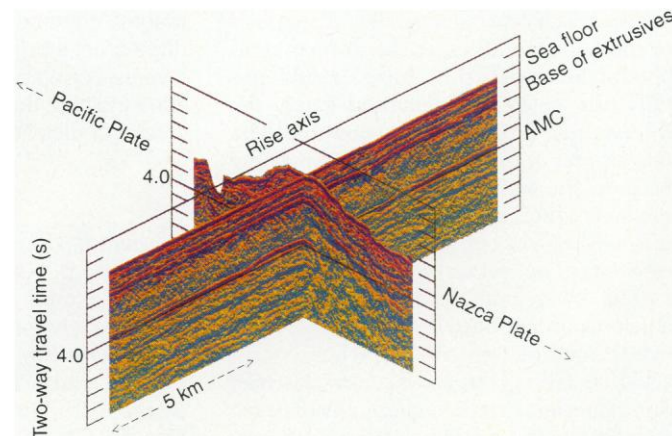


Fig. 2. Plot of two intersecting multichannel reflection profiles that were shot across and along the crest of the southern EPR near 14°14'S. Amplitudes are color coded: red indicates the highest amplitudes and blues indicate lower amplitudes. The event that marks the base of the extrusives along the rise axis has a relatively uniform thickness and shows rapid thickening off axis. A reflection from the roof of an axial magma body that underlies the rise axis occurs at ~4 s (~1 km) below the sea floor. This thin magma still is narrow (<1 to 2 km wide) across axis but remarkably continuous along the rise axis.



Vera and Diebold (19). This reflector has been attributed to diving rays that turn in the steep velocity gradient at the base of a surficial low-velocity layer (seismic layer 2A) that thickens rapidly off axis. This gradient is so steep that the event appears as a reflection in multichannel profiles, although it is actually observed only at wide offsets between shot and receiver. Along the southern EPR, this layer is <200 m thick at the rise axis and is associated with P-wave velocities of ≤ 2.5 km (Fig. 5). The base of this layer is marked by an abrupt velocity increase to >4.5 km s⁻¹, in some locations a second, smaller velocity discontinuity occurs below the first boundary.

The shallow crustal velocity structure of the southern EPR is strikingly similar to that reported from the northern EPR at both 9°N and 13°N on the basis of expanding-spread profiles (5, 19) (Fig. 5), on-bottom seismic refraction experiments (20), and tomographic studies (7, 8). The approximate doubling in thickness of the surficial low-velocity layer over an across-axis distance of only ~1 km is also similar to what has been reported from the northern EPR (17–20). This layer, which corresponds to seismic layer 2A, has been interpreted as lava flows that overlie sheeted dikes (7, 17, 20, 21) or as basalts with high

porosities that overlie basalts with lower porosities (2, 4). The thickening of this layer away from the ridge axis has been attributed to a progressive growth of the extrusive section by buildup of lava that overflows the axial summit caldera (7, 17, 20). However, in situ changes in porosity caused by hydrothermal circulation may contribute to the observed variation in thickness of this layer (9).

The high-amplitude reflector that lies ~450 ms below the sea floor at the rise axis in the 14°S area (Figs. 2 and 3) may be a reflection from the top of a narrow, thin melt sill similar to the one imaged along the northern EPR (3, 10, 11). This event can be directly tied to the top of an axial low-velocity zone that has been observed in rise-axis expanding-spread profiles (such as in Fig. 5) and in many locations is clearly phase-reversed relative to the reflection off of the sea floor. The 14°S profile shown in Figs. 2 and 3 is typical of how this event appears along much of the EPR south of the Garrett fracture zone. The reflector, and its associated diffractions, is up to 2 to 3 km wide on unmigrated time sections (Fig. 3). After time migration, the event collapses into a narrow (typically <1 km wide), flat-lying reflector that is usually located beneath the summit of the rise axis (Fig. 4).

Despite its narrow width, this reflector can be traced as a virtually continuous event for distances of many tens of kilometers in reflection profiles that were shot along the rise axis.

The shape of this event is similar to the reflection from the axial magma chamber (AMC) that has been observed along the northern EPR (3, 10, 11). The principal difference between the two areas is the generally more shallow depth of the AMC event along the southern EPR. Between 8°50'N and 13°30'N, this reflector typically lies 0.5 to 1.0 s below the sea floor. At 9°30'N, for example, the AMC reflector is located ~600 ms (1.6 km) below the sea floor (6, 11). In contrast, along the southern EPR this event commonly occurs <500 ms below the sea floor; at 14°14'S, for example, the AMC event lies ~450 ms below the sea floor (Figs. 2 and 3). Because the velocity structure of the crust that overlies the AMC is nearly identical on the northern and southern EPR (Fig. 5), this variation in two-way travel time represents a real difference in depth to the top of the melt lens. The median depth of this reflector along the EPR between the Garrett fracture zone and the 20.7°S propagator is ~1.3 km (530 ms) and in some locations (for example, 14°14'S and 17°25'S) it rises to within 1000 m of the sea floor.

A relatively continuous reflection ~1.8 s below the sea floor is interpreted as the Moho (Fig. 3). As was the case for the northern EPR (3), the Moho reflection can be traced within ~2 to 3 km of the rise axis on some profiles. The existence of a distinct seismic boundary between the crust and mantle suggests that their differentiation occurs at young ages (<40,000 years). Such early differentiation is predicted by crustal models in which the entire lower crustal gabbroic sequence forms primarily from material that flows downward and flankward from the thin, sill-like AMC (22, 23). The absence of a Moho reflection beneath the AMC may be due to the difficulty in imaging events that lie immediately below an attenuative, low-velocity body.

A series of reflection lines was shot along the crest of the EPR from just north of the 20.7°S propagator to the Garrett transform at 14°S in order to reveal along-axis variations in ridge-crest structure (Fig. 6). A seismic layer 2A event is present along almost the entire length of ridge we surveyed; the only areas where we did not image this event were in the immediate vicinity of several OSCs and along the ridge axis north of the 20.7°S propagator. The thickness of this near-surface, low-velocity layer is remarkably uniform along the rise axis, especially on the shallow, flat-topped ridge segment that lies between the Garrett transform and the 15°55'S OSC. The mean

Fig. 3. Larger scale plot of multichannel reflection profile shown in Fig. 2 that crosses the EPR near 14°14'S. The section is unmigrated and shows three prominent reflections: (i) a shallow reflector about 150 ms (<200 m) below the sea floor at the rise axis, interpreted as a reflection from the base of seismic layer 2A; (ii) a high-amplitude reflection that lies ~450 ms (~1 km) below the sea floor that is interpreted as a reflection from the top of a narrow, thin melt sill, and (iii) a relatively continuous reflector ~1.8 s below the sea-floor reflection that is interpreted as Moho and can be traced within ~2 to 3 km of the rise axis (<40,000-year-old crust).

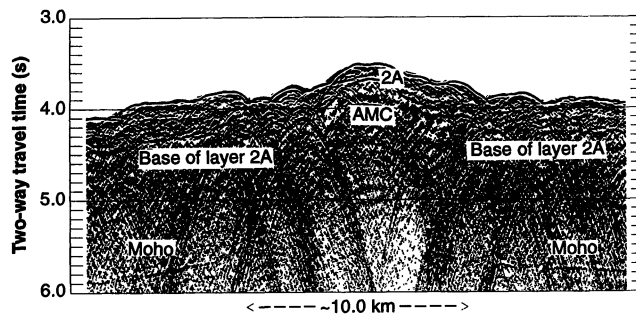
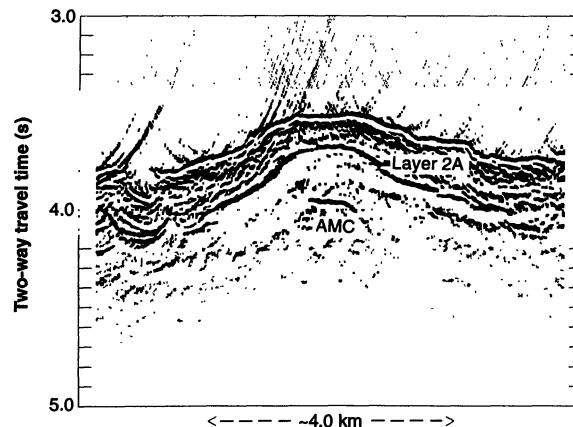


Fig. 4. Migrated version of the axial portion of the profile shown in Fig. 3 that shows the rapid off-axis thickening of the reflection from the base of layer 2A and the narrow (~800 m wide), flat-topped shape of the melt sill that underlies the axial region (AMC width, ~750 m). Migration was done with frequency wave number migration at 1500 m s⁻¹ and by the application of a 45° finite-difference residual migration (17). The velocity model that was used in the second step was based on the axial velocity structure shown in Fig. 5, adjusted for the variable thickness of layer 2A off-axis.



thickness of layer 2A along the entire 800-km section of the EPR between the Garrett fracture zone and the 20.7°S propagator is 147 ± 23 ms ($\sim 184 \pm 30$ m, on the assumption of an average velocity of 2.5 km s^{-1} for layer 2A). Between Garrett and the 15°55'S OSC, layer 2A has a mean thickness of 138 ± 11 ms ($\sim 173 \pm 15$ m). It was thinnest (~ 125 m) south of the 19°S OSC, along the ridge axis near 17°30'S, and south of Garrett fracture zone. It was thickest over the "hump" area between the 18°22'S and 18°37'S OSC (~ 260 m).

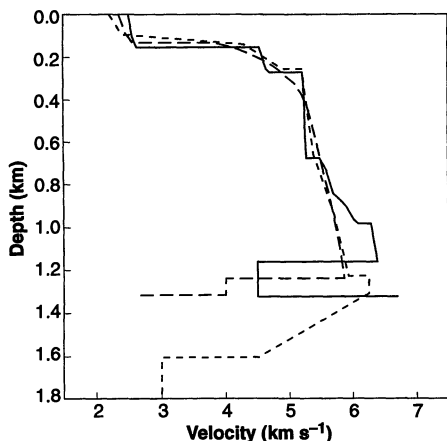


Fig. 5. Shallow crustal velocity structure (solid line) at the southern EPR from a two-ship expanding-spread profile that was shot along the rise crest at 17°09'S. This solution is considered representative of the axial velocity structure along the southern EPR. For comparison, velocity models are also shown for the slower spreading northern EPR at 9°N (6) (short dashes) and 13°N (5) (long dashes). Although there are differences in the depth of the axial low-velocity zone, the shallow crustal velocity structure in all three areas is remarkably similar.

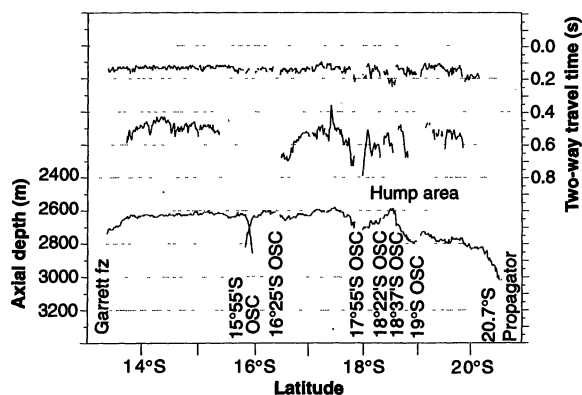
An AMC reflector was observed along $\sim 57\%$ of the ridge crest that was mapped between the Garrett fracture zone and the 20.7°S propagator, a frequency similar to that found along the slower spreading northern EPR (3). A nearly continuous AMC reflector can be mapped along the rise axis from 13°44'S to 15°23'S and from 16°31'S to 17°52'S (Fig. 6). The largest gap in the AMC event occurs north and south of the 15°55'S OSC. Such a reflector is also not observed along an ~ 90 -km length of ridge north of the 20.7°S propagator and in the immediate vicinity of several small OSCs between 17°55'S and 19°S. The AMC reflector is generally present where the ridge cross-sectional area is greatest, as predicted by Scheirer and Macdonald (24), although this relationship does not predict the large gap in the AMC event north and south of the 15°55'S OSC. Because it is difficult to keep the ship and streamer on the rise axis when the ridge axis rapidly changes trend (for example, near OSCs) a melt sill may be beneath some sections of the rise axis that are not indicated in Fig. 6.

There are significant variations in the two-way travel time of the AMC reflector in the along-axis reflection profiles shown in Fig. 6. The apparent deepening of the AMC event near the OSCs at 17°55'S, 18°22'S, 18°37'S, and 19°S is probably caused by diffractions from the edges of the narrow melt lens, a phenomenon that has been documented along the northern EPR (10). Thus, they do not reflect real variations in the depth of the AMC. However, away from these ridge-axis discontinuities are variations in AMC two-way travel times of >100 ms that are not correlated with off-axis wanderings of the ship track or changes in the thickness of layer 2A. These

variations, which may represent changes in the depth of the AMC, generally correlate well with the longer wavelength variations in the cross-sectional area of the ridge (24). The most shallow AMC event is near 17°25'S, where the axial reflector rises to within 360 ms (<900 m) of the sea floor over an along-axis distance of ~ 3 km. The rise axis at this location is shallow (<2600 m deep) and broad (24), and there is evidence from submersible observations and bottom photographs for recent eruptive activity in this area (25). The shallow melt lens at this location on the EPR may be a small magma chamber cupola that is associated with a recent or ongoing volcanic event. A broad, longer wavelength shallowing of the AMC reflector is also evident along the ridge segment between the Garrett fracture zone and the 15°55'S OSC, despite a relatively uniform thickness of layer 2A and nearly constant axial depths (Fig. 6). The AMC is most shallow (450 ms, or ~ 1 km below the sea floor) near 14°20'S and gradually deepens by nearly 100 ms (~ 225 m) over distances of 70 to 120 km north and south of this area before it disappears near the Garrett fracture zone and the 15°55'S OSC. These shallow AMC depths also correlate with broad sections of the EPR (24). With the exception of the extremely shallow event at 17°25'S, the AMC reflector is consistently more shallow along the portion of the ridge from Garrett to 15°55'S than elsewhere along the southern EPR, including the "hump" area between the 18°22'S and 18°37'S OSCs.

Our results here indicate few differences in axial structure between the northern and southern EPR despite spreading rates that differ by nearly 40%. If seismic layer 2A is interpreted as extrusive lava flows (7, 17, 19, 20), then the relatively constant thickness of this layer along the EPR suggests that the volume of extrusive lava produced at the EPR does not vary significantly with spreading rate. Our findings here also show that the size of crustal magma bodies does not strongly depend on spreading rate, as many ridge-crest thermal models have predicted. The magma sills that were observed on the intermediate-spreading (70 mm year $^{-1}$ full rate) Valu Fa Ridge in the Lau back-arc basin (26, 27) and on the faster spreading northern (120 mm year $^{-1}$) and southern EPR (150 to 162 mm year $^{-1}$) are all comparable in width (<1 to 4 km wide). However, our results do support a significant dependence of the depth of axial magma bodies on spreading rate (28), at least along intermediate- and fast-spreading ridges where the existence of these bodies is well documented. For example, on the Valu Fa Ridge the melt lens is ~ 3 to 3.5 km below the sea floor (26, 27), on the northern EPR the minimum depth range is typi-

Fig. 6. Summary of the regional variation in axial structure from the Garrett fracture zone at 13.4°S to the 20.7°S propagator, on the basis of seismic reflection profiles that were shot along the rise crest. The two upper curves plot the observed two-way travel time to the base of layer 2A and the AMC reflector, respectively. Axial depth is also plotted for reference in the lowest curve. Gaps in the 2A and AMC curves indicate portions of the rise axis where these events were not observed or, in a few cases mainly near OSCs, where the profile was clearly located off axis.



A reflection from the base of layer 2A is observed along almost this entire section of the southern EPR. The thickness of layer 2A is remarkably uniform, especially along the shallow, flat-topped ridge segment between the Garrett fracture zone and the 15°55'S OSC. The largest gaps in the AMC occur north and south of the 15°55'S OSC as well as near the Garrett fracture zone and the 20.7°S propagator. The melt lens is most shallow near 17°25'S, where it rises to within 360 ms (<900 m) of the sea floor, and along the rise axis south of the Garrett fracture zone near 14°20'S. The apparent deepening of the AMC event near many OSCs is probably due to imaging out-of-plane diffraction hyperbolas from the edge of the melt lens.

cally 1.3 to 1.6 km (3), and on the southern EPR the axial magma body appears to lie within 1 km below the sea floor in some areas. Phipps Morgan and Chen (22) have described conditions where the accumulation of melt in these bodies is controlled thermally by the balance of magmatic heat input and hydrothermal cooling. They have shown that under these conditions a variation in the depth of the axial melt lens with spreading rate is expected if the fraction of heat removed by hydrothermal circulation remains constant with spreading rate. Taken together, the results from our study provide strong additional support for the emerging view that crustal magma chambers along intermediate- and fast-spreading ocean ridges consist of small, sill-like mid-crustal bodies that overlie a broader, largely solidified lower crustal section.

REFERENCES AND NOTES

- The seismic structure of oceanic crust is typically divided into two major layers. The upper crust, layer 2, is characterized by a rapid increase in *P*-wave velocities from <2.5 to >6 km s⁻¹. Layer 2, which has a thickness of ~2 km, is sometimes subdivided into layers 2A, 2B, and 2C. The lower crust, layer 3, is about 5 km thick and is associated with much lower velocity gradients (<1 s⁻¹) and *P*-wave velocities of 6.5 to 7.0 km s⁻¹. The lithologic interpretation of this seismic layering is still not certain. However, layer 2 is generally believed to be made up of extrusive lava flows that grade downward into a sheeted dike complex, whereas layer 3 is interpreted as plutonic rocks such as gabbro, cumulate gabbro, and cumulate ultramafics.
- J. S. McClain, J. A. Orcutt, M. Burnett, *J. Geophys. Res.* **90**, 8627 (1985).
- R. S. Detrick *et al.*, *Nature* **326**, 35 (1987).
- M. S. Burnett, D. W. Caress, J. A. Orcutt, *ibid.* **339**, 206 (1989).
- A. J. Harding *et al.*, *J. Geophys. Res.* **94**, 12163 (1989).
- E. E. Vera *et al.*, *ibid.* **95**, 15529 (1990).
- D. R. Toomey, G. M. Purdy, S. C. Solomon, W. S. D. Wilcock, *Nature* **347**, 639 (1990).
- D. Caress, M. Burnett, J. Orcutt, *J. Geophys. Res.* **97**, 9243 (1992).
- W. S. D. Wilcock, S. C. Solomon, G. M. Purdy, D. R. Toomey, *Science* **258**, 1470 (1992).
- G. M. Kent, A. J. Harding, J. A. Orcutt, *Nature* **344**, 650 (1990).
- _____, in preparation.
- J. M. Sinton and R. S. Detrick, *J. Geophys. Res.* **97**, 197 (1992).
- C. DeMets, R. G. Gordon, D. F. Argus, S. Stein, *Geophys. J. Int.* **101**, 425 (1990).
- P. Lonsdale, *J. Geophys. Res.* **94**, 12197 (1989).
- K. C. Macdonald, R. M. Haymon, S. P. Miller, J.-C. Sempere, P. J. Fox, *ibid.* **93**, 2875 (1988).
- J. M. Sinton, S. M. Smaglik, J. J. Mahoney, K. C. Macdonald, *ibid.* **96**, 6133 (1991).
- A. J. Harding, G. M. Kent, J. A. Orcutt, *ibid.*, in press.
- A. J. Harding, G. M. Kent, M. E. Kappus, J. A. Orcutt, *Eos* **72**, 494 (1991).
- E. E. Vera and J. B. Diebold, *ibid.*, p. 495.
- G. L. Christeson, G. M. Purdy, G. J. Fryer, *Geophys. Res. Lett.* **19**, 1045 (1992).
- T. J. Herron, *ibid.* **9**, 17 (1982).
- J. Phipps Morgan and Y. J. Chen, *Eos* **73**, 290 (1992).
- T. J. Henstock, A. W. Woods, R. S. White, *J. Geophys. Res.*, in press.
- D. S. Scheirer and K. C. Macdonald, *Eos* **72**, 506 (1991).
- V. Renard, R. Hekinian, J. Francheteau, R. D. Ballard, H. Backer, *Earth Planet. Sci. Lett.* **75**, 339 (1985).
- J. L. Morton and N. Sleep, in *Geology and Offshore Resources of Pacific Island Arcs—Tonga Region*, D. W. Scholl and T. L. Vallier, Eds. (Circum-Pacific Council for Energy and Mineral Resources, Houston, TX, 1985), pp. 441–453.
- J. Collier and M. Sinha, *Nature* **346**, 646 (1990).
- G. M. Purdy, L. S. L. Kong, G. L. Christeson, S. C. Solomon, *ibid.* **355**, 815 (1992).
- We thank the officers, crew, and scientific com-

plement of the research vessels *Maurice Ewing* and *Thomas Washington* for their expert help in collecting these data. Supported by the Ridge Inter Disciplinary Global Experiments program through funds provided by the National Science Foundation to Lamont-Doherty Geological Observatory, Scripps Institution of Oceanography, and Woods Hole Oceanographic Institution and by Woods Hole Oceanographic Institution contribution 8204.

31 August 1992; accepted 20 November 1992

In Situ Stimulation of Aerobic PCB Biodegradation in Hudson River Sediments

M. R. Harkness, J. B. McDermott, D. A. Abramowicz,* J. J. Salvo, W. P. Flanagan, M. L. Stephens, F. J. Mondello, R. J. May, J. H. Lobos, K. M. Carroll, M. J. Brennan, A. A. Bracco, K. M. Fish, G. L. Warner, P. R. Wilson, D. K. Dietrich, D. T. Lin, C. B. Morgan, W. L. Gately

A 73-day field study of in situ aerobic biodegradation of polychlorinated biphenyls (PCBs) in the Hudson River shows that indigenous aerobic microorganisms can degrade the lightly chlorinated PCBs present in these sediments. Addition of inorganic nutrients, biphenyl, and oxygen enhanced PCB biodegradation, as indicated both by a 37 to 55 percent loss of PCBs and by the production of chlorobenzoates, intermediates in the PCB biodegradation pathway. Repeated inoculation with a purified PCB-degrading bacterium failed to improve biodegradative activity. Biodegradation was also observed under mixed but unamended conditions, which suggests that this process may occur commonly in river sediments, with implications for PCB fate models and risk assessments.

Polychlorinated biphenyls undergo biodegradation under a variety of conditions in the laboratory and in aquatic sediments (1, 2). Two classes of bacteria with PCB-transforming capabilities have been identified. Anaerobic bacteria that dechlorinate PCBs typically attack the higher chlorinated PCB congeners through reductive dechlorination (3), a process that removes chlorines but leaves the biphenyl rings intact. This process has occurred extensively in a number of sediments (3–5), which results in a reduction in higher chlorinated PCB congeners and a commensurate increase in lower chlorinated congeners. Similar selective shifts in PCB congener distributions have been reproduced in laboratory experiments with anaerobic sediment slurries that contained active microbial populations (6, 7).

The less chlorinated PCB congeners produced by anaerobic dechlorination are suitable substrates for oxidative degradation by a wide range of aerobic organisms (8–12). The predominant mechanism in the enzymatic pathway for oxidative PCB biodegradation involves an initial 2,3-dioxygenase attack, followed by oxidation through a second dioxygenase and ring cleavage (8). Products of

this pathway include the corresponding chlorobenzoic acids, which are readily degraded by other aerobic bacteria (13, 14).

Although much is known about the oxidative degradation of PCBs by aerobic bacteria in laboratory experiments (1, 2), little is known about this process in the field. To that end we performed an in situ PCB bioremediation experiment in a river sediment environment. The objectives of the study were to demonstrate that aerobic PCB biodegradation can occur under field conditions and to identify the key variables that influence the rate and extent of PCB biodegradation in Hudson River sediments.

Several criteria were used to assess the extent to which in situ biodegradation is responsible for PCB losses in Hudson River sediments (15): (i) the use of controls to distinguish between biotic and abiotic losses, (ii) quantitation of the loss of co-reactants that participate in the biodegradation process (O₂ and biphenyl), (iii) enumeration of PCB-degrading microbial populations that correlate with in situ biodegradation, (iv) observation of the selective disappearance of microbially labile PCB congeners, and (v) detection of metabolic intermediates (chlorobenzoates).

The field study was conducted immediately offshore from the west bank of the Hudson River in the town of Moreau, New

GE Corporate Research and Development Center, Schenectady, NY 12301.

*To whom correspondence should be addressed.